Available online at www.sciencedirect.com
ScienceDirect
International Journal of Heat and Fluid Flow 27 (2006) 756–767
International Journal of HEAT AND FLUID FLOW
www.elsevier.com/locate/ijhff

Turbulence modelling of statistically periodic flows: Synthetic jet into quiescent air

S. Carpy, R. Manceau *

Laboratoire d'Études Aérodynamiques, UMR 6609, CNRS/University of Poitiers/ENSMA, SP2MI, Boulevard Marie et Pierre Curie, Téléport 2 – BP 30179 - 86962 Futuroscope Chasseneuil Cedex, France

Received 14 October 2005; received in revised form 23 January 2006; accepted 4 April 2006
Available online 30 June 2006

Abstract

Computations of a 2D synthetic jet are performed with usual RANS equations solved in time-accurate mode (URANS), with the standard k–ε model and the Rotta + IP second moment closure. The purpose of the present work is to investigate the ability of these standard turbulence models to close the phase-averaged Navier–Stokes equations. Results are compared with recent experiments by Yao et al. made available to the CFD Validation of Synthetic Jets and Turbulent Separation Control workshop held in Williamsburg in 2004. Comparisons of the performance of the models with experimental data show that the evolution of the vortex dipole generated by inviscid mechanisms is not correctly reproduced by the k–ε model. The Reynolds-stress model gives much more realistic predictions. However, several characteristics are not well predicted, as for instance the convection velocity. A detailed analysis shows that the vortex dipole dynamics is essentially inviscid during the early blowing phase, when the flow is more transitional than fully turbulent. Turbulence develops and influences the dynamics of the vortices only at a later stage of the blowing phase. Consequently, it is of importance that the turbulence models do not predict erroneously high levels of turbulence. In particular, the present study shows that the correct prediction of the region of negative production that appears during the deceleration of the blowing velocity, due to the misalignment of the strain and anisotropy tensors, is crucial. Therefore, linear eddy-viscosity models must be discarded for this type of pulsed flows, in particular for flow control using synthetic jets.

Keywords: Turbulence modelling; URANS; Synthetic jet; Statistical unsteadiness; Control

1. Introduction

Although statistical turbulence modelling (RANS) represents the current industrial standard, there is a considerable interest in the possibility of obtaining informations on the large-scale unsteadiness. As long as Large Eddy Simulation will remain too expensive for overnight simulations, some room exists for the development of less expensive methods able to predict the very large scales of the flow. This type of approaches has important applications in different domains: among others, aeronautics (Gatski, 2001; Jin and Braza, 1994), control (Getin, 2000; Hassan and Janakiram, 1997), aeroacoustics (Bastin et al., 1997), power generation (Benhamadouche and Laurence, 2003) and environment (Kenjereš et al., 2005, 2001) can be cited.

In many statistically steady flows, as soon as the time derivatives are included in the equations, unsteady RANS solutions appear naturally (Johansson et al., 1993; Bosch and Rodi, 1996; Benhamadouche and Laurence, 2003; Jin and Braza, 1994; Lasher and Taulbee, 1992; Iaccarino and Durbin, 2000). In such cases, long-time-averaged solutions are often better than solutions obtained by steady-state computations (Durbin, 1995; Iaccarino and Durbin, 2000). However, there is no clear consensus on the definition of the mean operator for this type of computations: the definition of the turbulent scales resolved by the method is not a priori known. Recent approaches, like

* Corresponding author. Tel.: +33 549 496 927; fax: +33 549 496 968.
E-mail address: remi.manceau@lea.univ-poitiers.fr (R. Manceau).

0142-727X/$ - see front matter © 2006 Elsevier Inc. All rights reserved.
doi:10.1016/j.ijheatfluidflow.2006.04.002

Nomenclature

$\bar{\cdot}$	long-time averaging operator	ν''_T	turbulent viscosity
$\langle\cdot\rangle$	phase averaging operator	δ_{ij}	Kronecker symbol
u_i^*	instantaneous velocity	ρ	density of air
p^*	instantaneous pressure	f	frequency of the jet
$U_i = \overline{u_i^*}$	long-time-averaged velocity	h	width of the slot
$\widetilde{U}_i = \langle u_i^* \rangle$	phase-averaged velocity	$P_{k''}$	production of turbulent kinetic energy
$u_i'' = u_i^* - \widetilde{U}_i$	fluctuation around phase-averaged velocities	$\underline{\underline{a}}''$	anisotropy tensor $a''_{ij} = \langle u_i'' u_j'' \rangle / k'' - \frac{2}{3}\delta_{ij}$
$\langle u_i'' u_j'' \rangle$	Reynolds stresses	Γ	circulation
$k'' = \frac{1}{2}\langle u_i'' u_i'' \rangle$	turbulent kinetic energy	$\widetilde{\omega}$	phase-averaged vorticity in the z-direction $\widetilde{\omega} = \nabla \times \underline{\widetilde{U}}$
ε''	dissipation rate of k''	λ_i	eigenvalues of $\underline{\underline{a}}''$
$\underline{\underline{\widetilde{S}}}$	strain-rate tensor $\widetilde{S}_{ij} = \frac{1}{2}(\frac{\partial \widetilde{U}_i}{\partial x_i} + \frac{\partial \widetilde{U}_i}{\partial x_i})$	β	positive eigenvalue of $\underline{\underline{\widetilde{S}}}$

Semi-Deterministic Modelling (SDM: Ha Minnh and Kourta, 1993; Aubrun et al., 1999; Bastin et al., 1997), Very-Large-Eddy Simulation (VLES: Speziale, 1998), Detached-Eddy Simulation (DES: Spalart et al., 1997), Limited Scales simulations (LNS: Batten et al., 2002), Scale-Adaptative Simulation (SAS: Menter and Egorov, 2005), Partially-averaged Navier–Stokes modelling (PANS: Girimaji et al., 2003) or Partially-integrated Transport modelling (PITM: Chaouat and Schiestel, 2005; Schiestel and Dejoan, 2005) are designed in order to ensure unsteady solutions.

In the present study, the flow belongs to the class of statistically periodic flows, i.e., flows in which the boundary conditions are periodic in time. The use of RANS models does not raise any theoretical issue in this case, since Reynolds average is equivalent to phase average. However, obtaining a periodic solution is not guaranteed: some frequencies can appear that are not harmonics of the forcing frequency.

Moreover, while the relative performance of the numerous turbulence models available have been investigated extensively in statistically steady flows, their ability to close successfully the phase-averaged equations in periodic flows have received much less attention, and generally for modified versions of the models (Tardu and Da Costa, 2005; Stawiarski and Hanjalić, 2002; Bremhorst et al., 2003; Lardeau and Leschziner, 2005). Therefore, a workshop dedicated to the evaluation of modelling strategies in statistically periodic flows was recently organized (Rumsey et al., 2004; Sellers and Rumsey, 2004). The present study focuses on the comparison of the performance of first and second moment closures: the standard k–ε model (Launder and Spalding, 1974) and the Rotta + IP second moment closure (Launder et al., 1975) are used, without any case-specific modification. Standard wall functions are applied since near-wall regions do not play a significant role.

The flow studied in the present article is one of the test cases selected for the workshop. The flow consists in an oscillatory jet with zero-net-mass flow issuing into quiescent air. This flow is of high industrial interest, in particular in the frame of turbulence control, since it is representative of MEMS piezoelectric technology, as developed by Seifert et al. (1993) and Amitay et al. (2001).

Separation control through the use of suction, blowing and periodic excitation has lead to a number of studies (see, e.g., the review by Greenblatt and Wygnanski, 2000). The present case was designed in order to evaluate the capabilities of CFD and modelling techniques in this type of problems, concentrating on the synthetic jet region, without interaction with an outer flow. The experiments used as reference were performed at NASA LaRC by Yao et al. (2004) and are available on the web site of the workshop (Sellers and Rumsey, 2004).

In such a problem, it is convenient to introduce two averaging operators: long-time averaging, denoted by $\bar{\cdot}$ and phase (or ensemble) averaging, denoted by $\langle\cdot\rangle$. Instantaneous quantities are denoted by stars (u_i^*, p^*) and the following definitions are used:

$$\text{Long-time-averaged velocity:} \quad U_i = \overline{u_i^*}$$

$$\text{Phase-averaged velocity:} \quad \widetilde{U}_i = \langle u_i^* \rangle$$

In order to avoid confusion with usual notation in RANS modelling, where u_i' stand for the total fluctuations (around the long-time-averaged velocities), the fluctuations around phase-averaged velocities are denoted by u_i'':

$$u_i'' = u_i^* - \langle u_i^* \rangle \tag{1}$$

Thus, in the present periodic case, the transport equations to be solved are those of the phase-averaged velocity components $\widetilde{U}_i$:

$$\frac{\partial \widetilde{U}_i}{\partial t} + \widetilde{U}_j \frac{\partial \widetilde{U}_i}{\partial x_j} = -\frac{1}{\rho}\frac{\partial \widetilde{P}}{\partial x_i} + \nu \frac{\partial^2 \widetilde{U}_i}{\partial x_j \partial x_j} - \frac{\partial \langle u_i'' u_j'' \rangle}{\partial x_j} \tag{2}$$

and those of the Reynolds stresses $\langle u_i'' u_j'' \rangle$ (or of $k'' = \frac{1}{2}\langle u_i'' u_i'' \rangle$ in the frame of the eddy-viscosity model), and of ε'', the dissipation rate of k'': all these equations are formally identical to the standard steady RANS equations, except for the presence of the time derivative.

In order to close the equations, two different standard turbulence models are used: the standard k–ε model (Launder and Spalding, 1974), denoted k''–ε'' in the present case, and the Rotta + IP Reynolds-stress model (Launder et al., 1975).

2. Description of the geometry and available experimental data

The oscillating jet of air emanates from a slot in the floor. The slot is $h = 1.27$ mm wide and $28h$ long, in order to produce a 2D plane jet. The slot is at the bottom of a cubic enclosed box $480h = 609.6$ mm large, at the centre of the floor and parallel to the outer walls. The geometry and the coordinate system are shown in Fig. 1.

The jet is produced by a piezo-electric diaphragm on the side of a narrow cavity under the floor, which is driven at 444.7 Hz (Sellers and Rumsey, 2004). The maximum jet velocity generated could reach 28 m s^{-1}.

Although the actuator operating parameters including diaphragm displacement, internal cavity pressure, and internal cavity temperature were monitored to provide boundary conditions for CFD simulations, we chose not to solve the flow in the cavity: the present work focuses on the performance of turbulence models, rather than on the other difficult issue of representing a vibrating diaphragm with simple boundary conditions.

Computational results in the present article are compared with the PIV measurements performed by Yao et al. (2004). Phase-averaged (every 5°) and long-time-averaged velocities and Reynolds stresses (only components in the x–y plane) are available in the window $-2.15 < x/h < 3.1$, $0.1 < y/h < 6.6$, $z = 0$, corresponding, in actual size, to -2.73 mm $< x < 3.94$ mm, 0.127 mm $< y <$ 8.38 mm.

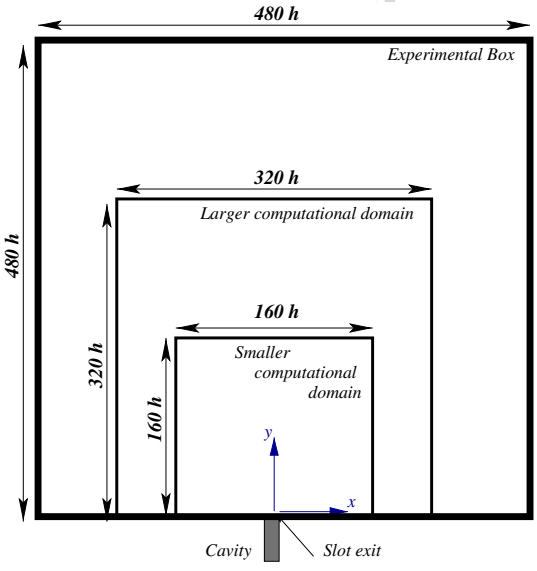

Fig. 1. Geometry, domain size and coordinate system.

3. Numerical method and sensitivity studies

Computations are performed using *Code_Saturne*, a finite volume solver on unstructured grids developed at EDF (Archambeau et al., 2004), for vectorial and parallel computing.

The code solves time-dependent RANS or LES equations for Newtonian incompressible flows. Space discretization is based on the collocation of all the variables at the centre of gravity of the cells. Velocity/pressure coupling is ensured by the SIMPLEC algorithm, with the Rhie and Chow interpolation in the pressure-correction step. The Poisson equation is solved using a conjugate gradient method, with diagonal preconditioning. The present study is performed using the usual standard k–ε model (Launder and Spalding, 1974) and the Rotta + IP second moment closure (Launder et al., 1975). Central differencing is used for convection. For time-marching, a second order Crank–Nicholson scheme is used for the k–ε model and, for stability reasons, a first-order Euler implicit scheme for the Reynolds-stress model. However, as shown below, time-step-independent solutions are reached in all cases. Computations are performed on 8 processors of a PC cluster.

3.1. Boundary conditions

Since the flow inside the cavity is not solved, unsteady Dirichlet boundary conditions are specified at the slot exit (Fig. 2), which are functions of x and phase: profiles at $y/h = 0.079$ of the available phase-averaged velocities $\widetilde{U}_i$ and Reynolds stresses $\langle u_i'' u_j'' \rangle$ are extracted from PIV data and used as inlet conditions. The missing component $\langle w''^2 \rangle$ is reconstructed by assuming $\langle w''^2 \rangle = \langle u''^2 \rangle$.

Concerning the dissipation rate ε'', prescribing an inlet value is already an issue. Indeed, ε'' obviously varies with time, as well as all the other usual turbulent scales (time scale, length scale, eddy-viscosity). A possible way is to arbitrarily assume that one of them is constant, e.g., the length scale L. A periodic ε'' can thus be obtained from

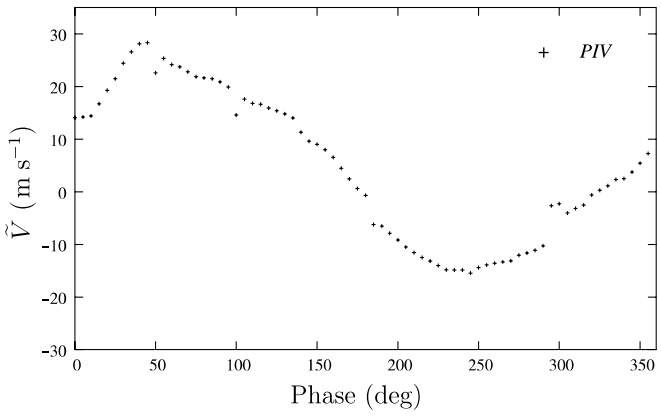

Fig. 2. Measured vertical velocity over the centre of the slot as a function of phase ($x/h = 0$, $y/h = 0.079$).

$\varepsilon'' = k''^{3/2}/L$. Preliminary computations (not shown here) have indicated that a value of L of the order of magnitude of what can be expected in a fully developed turbulent channel flow (typically one-tenth of the half-width of the slot) gives too much turbulent dissipation. Therefore, the value of the length scale prescribed in the computations presented here is half the slot width. The necessity of using such a large value is to be linked to the fact that, despite a turbulence rate of 5%, the flow issuing from the cavity is far from being a fully developed turbulent flow: the Reynolds number based on the slot width and the maximum inlet velocity is only 2400, and the geometry of the cavity does not allow the turbulence to reach a spectral equilibrium before issuing from the slot.

Solid-wall boundary conditions cannot be used at the remaining boundaries of the domain, since the fluid is considered incompressible: when fluid is blown from the slot, it is necessary to enable an equivalent volume of fluid to go out of the calculation domain in order to satisfy incompressibility. Since the experimental box is huge compared to the size of the slot ($480h$), a smaller domain was used, as shown in Fig. 1. Outlet boundary conditions (homogeneous Neuman conditions) are applied at the open boundaries of the domain: as shown in Section 3.3, the results are not influenced by this restriction of the domain. However, in this type of flows, fluid enters the domain through the "outlet boundaries" in different regions, at different periods of the cycle, in particular during suction: everywhere the mass flux enters the domain, Dirichlet boundary conditions are used for turbulent quantities, using values identical to those used for the initial conditions described just below.

Note that the symmetry of the flow is not imposed in this study, in order to enable the appearance of non-symmetrical solutions. However, only symmetrical solutions have been obtained.

3.2. Initial conditions

Computations are started from rest state ($\widetilde{U}_i = 0$), with a low residual turbulent energy ($k''^{1/2}/\widetilde{V}_{\max} = 0.05\%$) and a dissipation rate corresponding to the ratio $\nu_t/\nu = 10$. Computations are directly started with central differencing with large time steps (Δt corresponding to $\Delta\phi = 2.5°$), which shows the stability of the code (for convenience, time steps are given in phase degrees $\Delta\phi$ throughout the article, i.e., the value corresponds to $\Delta\phi = 360 f \Delta t$, where f is the frequency of the jet, such that $\Delta\phi = 360°$ corresponds to a cycle). When a satisfactory periodic state is reached (after about 15 cycles), the time step is reduced and the computation is run until a new periodic state is obtained. Note that periodicity was only evaluated in the region where the flow is of interest (basically the region in which the results can be compared with experiments): indeed, it would take hundreds of cycles to reach a periodic solution in the entire domain.

3.3. Sensitivity studies

In order to investigate the influence of the size of the domain, the time-step and the grid, seven different computations were performed with the standard k''–ε'' model and the Rotta + IP second moment closure. Conclusions are given below.

3.3.1. Influence of the domain size

k''–ε'' computations were performed using two different domain sizes (small and large, Fig. 1) with the same grid resolution (i.e., for the larger domain, cells were added around the grid used for the smaller domain). The grid covering the smaller domain is shown in Fig. 3a. Computations were carried out with the same time step corresponding to $\Delta\phi = 2.5°$, i.e., 144 time steps per cycle. Fig. 4a clearly shows that the restriction of the domain has no influence on the solution. Therefore, the smaller domain in used in the following of the article.

3.3.2. Influence of the time step

The influence of the time-step on the solution has been carefully investigated. Using the coarse grid in the smaller domain, the time step was progressively reduced: for the k''–ε'' model (second-order time-marching scheme), the solution becomes independent of the time step below a value of 0.5° (see Fig. 4b). This conclusion was confirmed using the fine grid. For the Reynolds-stress model (first-order time-marching scheme), the time-step independence is reached at 0.25°, i.e., 1440 time steps per cycle. It is worth

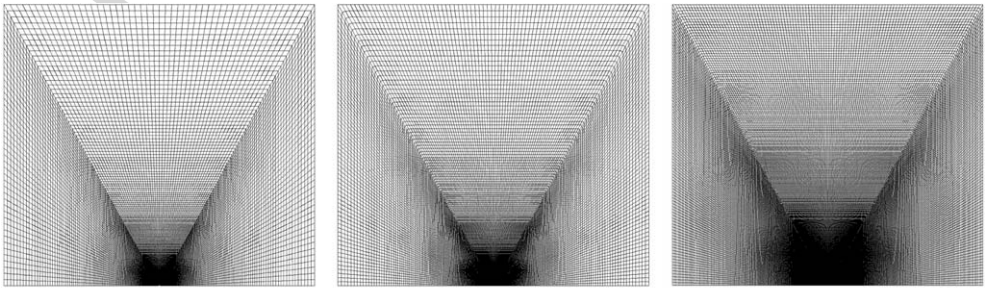

(a) coarse grid (b) middle grid (c) fine grid

Fig. 3. Computational grids.

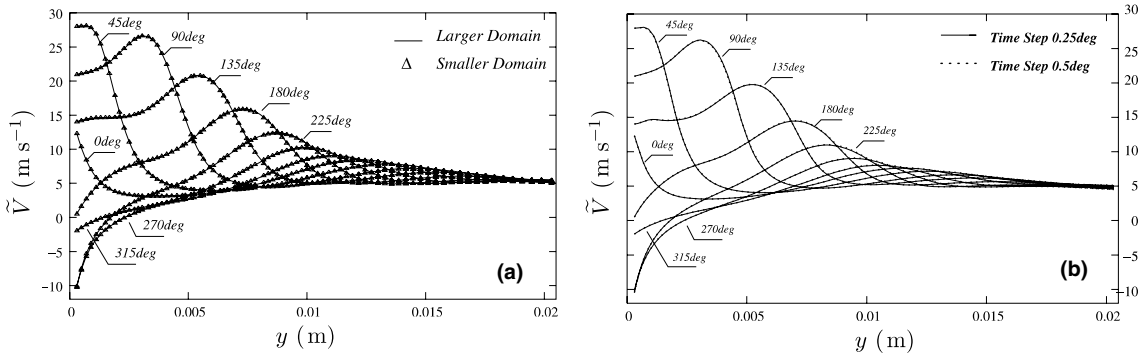

Fig. 4. Influence of the size of the domain (a) and of the time step (b). Velocity profiles in the symmetry plane at different phase angles. k''–ε'' model.

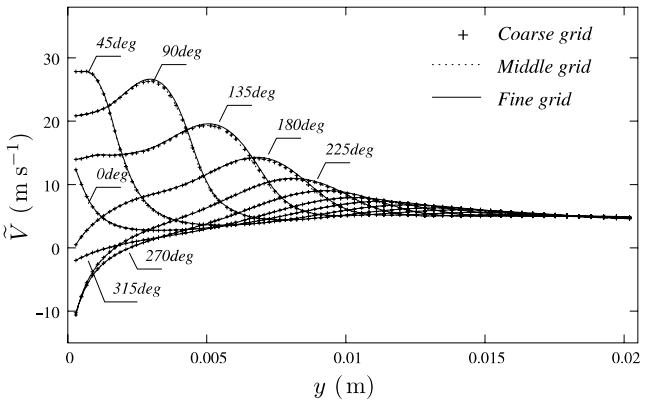

Fig. 5. Influence of the grid. Velocity profiles in the symmetry plane at different phase angles. k''–ε'' model.

pointing out that reaching a time-step-independent solution requires a large number of time steps per cycle. In a recent study, Lardeau and Leschziner (2005) showed that the solution obtained by URANS in the case of a flow around a cylinder is qualitatively modified (from a quasi-steady solution to a vortex street) when the time step is reduced: at least 125 time steps per cycle are necessary to properly obtain the vortex shedding. The present study indicates that a true time-step independence is actually much more demanding.

3.3.3. Grid refinement

Three different grids (coarse grid: 32900 cells, middle grid: 47610 cells, fine grid: 130950 cells), shown in Fig. 3, are used. Fig. 5 shows that the influence of the grid refinement is small (the discrepancies between the middle grid and the fine grid are of the order of 1%). Therefore, all the results presented in the following of the article were obtained using the middle grid.

4. Results and discussion

4.1. Global characteristics of the flow

Figs. 7 and 8 show comparisons of the isocontours of the vertical phase-averaged velocity $\widetilde{V}$ from PIV measurements, k''–ε'' and RSM computations, for both blowing and suction phases of the cycle (see Fig. 2). It can be seen that the global topology of the phase-averaged flow is well reproduced by both models. It is first worth pointing out that the turbulence models play the role that is expected in this type of flow: the resolved velocity field $\widetilde{V}_i$ is free from turbulent eddies and $\widetilde{V}_i$ only represents the oscillating motion induced by the diaphragm.

The pair of large vortices (Fig. 7) that appears at the beginning of the blowing phase is directly inherited from inviscid dynamics: it is induced by the vorticity injected into the domain through the slot (see Section 4.4). However, even though the turbulence models do not play a role in their creation, the turbulence field has a significant influence on their evolution into the domain, and the Reynolds-stress model produces a much more realistic picture. The k''–ε'' model is much too diffusive as can be observed in Fig. 6. The vortices are dissipated very rapidly, as seen in the movies that can be found on a dedicated website (Carpy and Manceau, 2006).

Fig. 6 shows profiles in the symmetry plane of the phase-averaged velocity $\widetilde{V}$. It appears that the k''–ε'' model predicts a much too rapid decrease of the peak velocity, and, in particular, is unable to reproduce the acceleration above the slot which is observed in the PIV data: the velocity at the slot exit reaches its maximum 28.3 m s^{-1} at phase 45

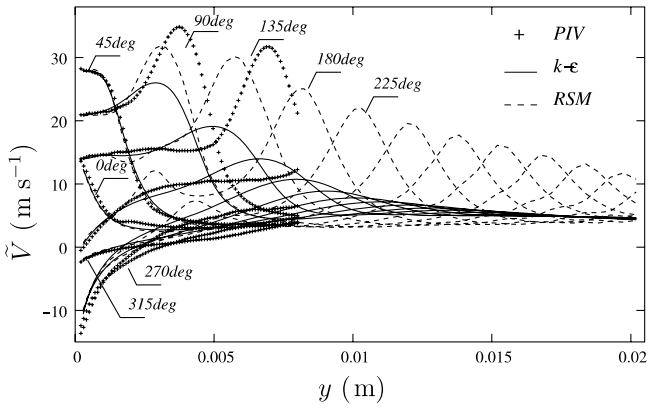

Fig. 6. Comparisons of velocity profiles in the symmetry plane at different phase angles.

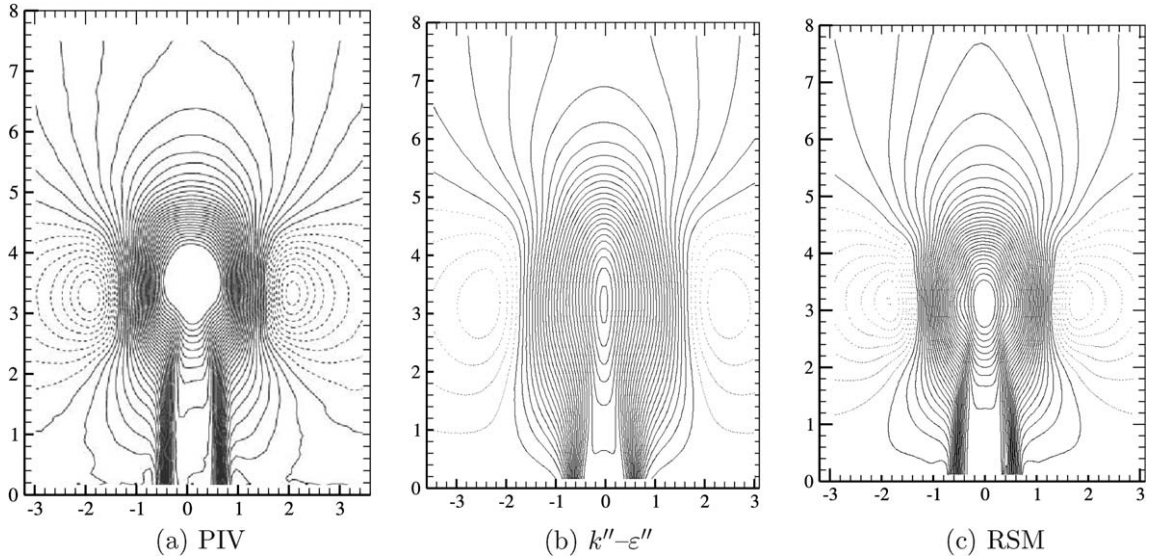

Fig. 7. Contours of phase-averaged velocity $\widetilde{V}$ at phase 90 (blowing). Dashed lines = negative contours.

(see Fig. 2) and, at phase 90, the peak velocity at about $y = 4$ mm (3.15h) is close to 35 m s^{-1}. The "fluid particle" with the maximum velocity at phase 90 has been experiencing an acceleration since it issued from the slot. Fig. 6 shows that this behaviour is reproduced, but underestimated, by the Reynolds-stress model. In both cases, the convection velocity of the peak is underestimated (Figs. 6 and 7). The misprediction of the peak velocity and of the convection velocity are both due to the overestimation of the turbulence intensity, which is particularly severe with the k''–ε'' model, as will be shown in the following sections.

During the suction phase of the cycle, Fig. 8 shows that the fluid is mainly sucked from the sides. This is the main explanation (apart from experimental errors) of the fact that, in Fig. 2, the integral of the curve is not zero: what is plotted is the velocity at the centre of the slot, at the elevation $y = 0.08h$. Since fluid is mainly blown at the centre of the slot and sucked from the sides, a very significant part of the fluid that enters the cavity during the suction phase is not seen at that point. Therefore, computations cannot be performed using uniform profiles (independent of x): if the flow in the internal cavity is not solved, it is necessary to base the inlet conditions on profiles extracted from the PIV velocity fields, as is done in the present study.

This characteristic behaviour of the flow is confirmed by Fig. 9, in which long-time-averaged velocity fields are shown. It clearly appears that the fluid tends to issue from the cavity at the centre of the slot and to enter from the sides. Both models (eddy-viscosity and Reynolds-stress models) correctly reproduce this behaviour.

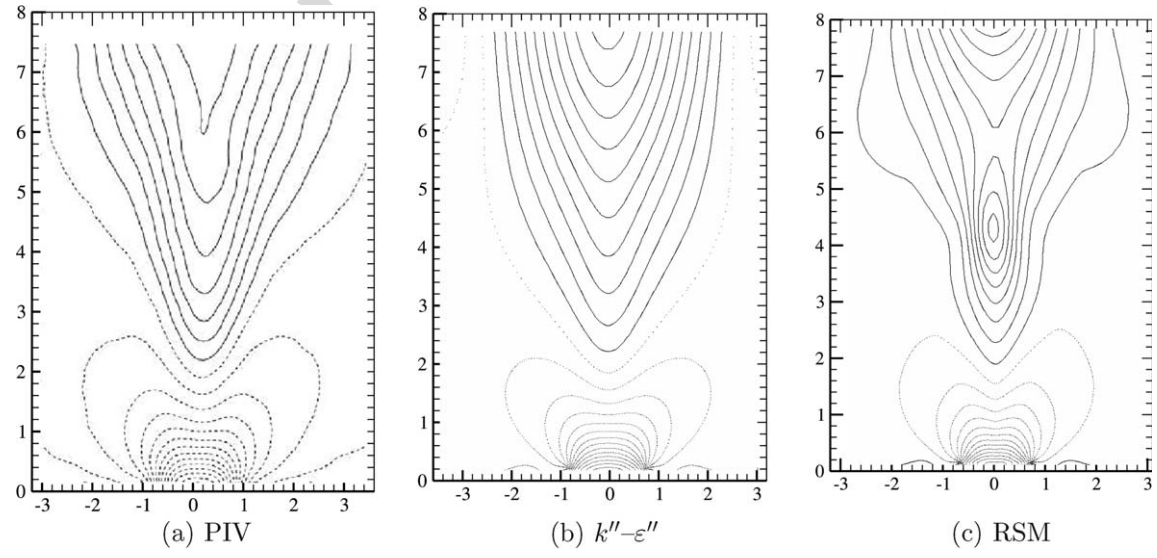

Fig. 8. Contours of phase-averaged velocity $\widetilde{V}$ at phase 225 (suction). Dashed lines = negative contours.

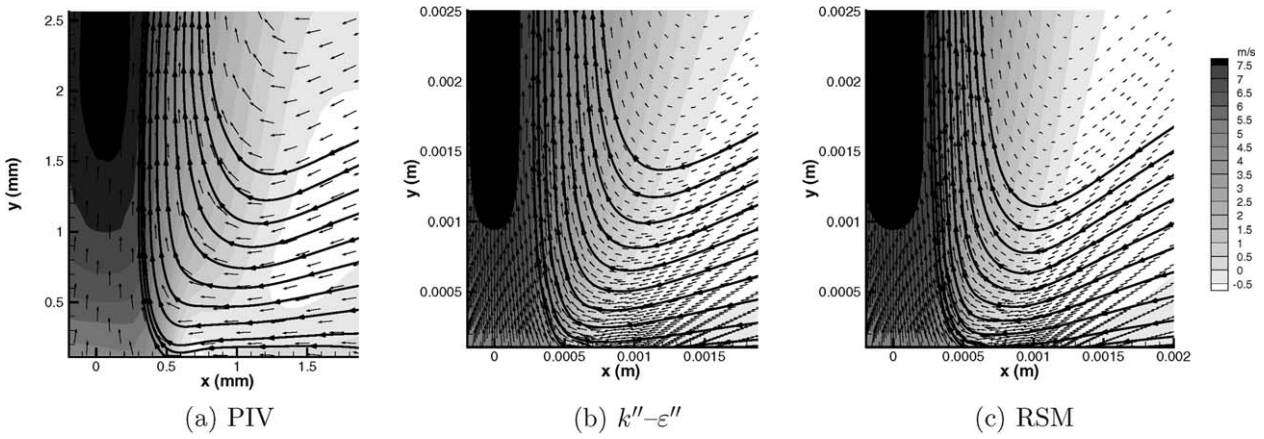

Fig. 9. Contours, vectors and streamlines of long-time-averaged velocity.

4.2. Momentum budget

In order to investigate the discrepancies between the two models, it is convenient to focus on the material derivative of the velocity *in the symmetry plane* $x = 0$:

$$\frac{\mathrm{d}\widetilde{V}}{\mathrm{d}t} = -\frac{1}{\rho}\frac{\partial \widetilde{P}}{\partial y} - \frac{\partial \langle v''^2\rangle}{\partial y} - \frac{\partial \langle u''v''\rangle}{\partial x} + \nu\frac{\partial^2 \widetilde{V}}{\partial x_k \partial x_k} \tag{3}$$

The acceleration of the fluid particle described above results from a competition between the first three terms on the right hand side (pressure gradient and Reynolds stresses), since the molecular diffusion is negligible. The main difference between the two models obviously lies in the Reynolds-stress tensor, and in particular in the prediction of the sign of the contribution of normal stress $\langle v''^2\rangle$: the shear stress $\langle u''v''\rangle$ is globally well reproduced by both models, and always contributes as a sink in Eq. (3).

Figs. 10 and 14 show that the Reynolds-stress model predicts a region of negative production right above the slot: in the present 2D case, using the incompressibility condition, the production of k'' reduces to:

$$P_{k''} = \langle u''^2\rangle\frac{\partial V}{\partial y} - \langle v''^2\rangle\frac{\partial V}{\partial y} - \langle u''v''\rangle\left(\frac{\partial U}{\partial y} + \frac{\partial V}{\partial x}\right) \tag{4}$$

In the symmetry plane, the last term is zero because $\langle u''v''\rangle = 0$. Fig. 10 shows that the first term is positive and the second term is negative. This is a direct consequence of the unsteadiness of the boundary conditions. Indeed, since the velocity at the slot exit decreases rapidly after phase 45 (Fig. 11, arrows a and b), the partial derivative $\partial V/\partial y$ at phases >45° is positive between the slot exit ($y = 0$ mm) and the location of the peak velocity (Fig. 11, arrows c and d): for instance, it is seen that at phase 90, $\partial V/\partial y$ is positive between $y = 0$ mm and $y \simeq 4$ mm. Therefore, *in or close to the symmetry plane*, the second term in the RHS of Eq. (4) is necessarily negative, and leads to a decrease of $\langle v''^2\rangle$, since this term is actually $\frac{1}{2}P_{22}$. This mechanism, due to a locally positive streamwise velocity gradient, similarly to the case of the flow in a convergent nozzle, can be expected in many unsteady flows, in particular in pulsed jets.

On the contrary, the first term, which is $\frac{1}{2}P_{11}$, is positive. The production of k'' is negative because $\langle v''^2\rangle$ is larger than $\langle u''^2\rangle$ in the jet.

This phenomenon was observed in the far field of a transient axisymmetric turbulent jet submitted to a large and sudden decrease in its ejection velocity (Borée et al., 1997). During the velocity decrease, analysis of the

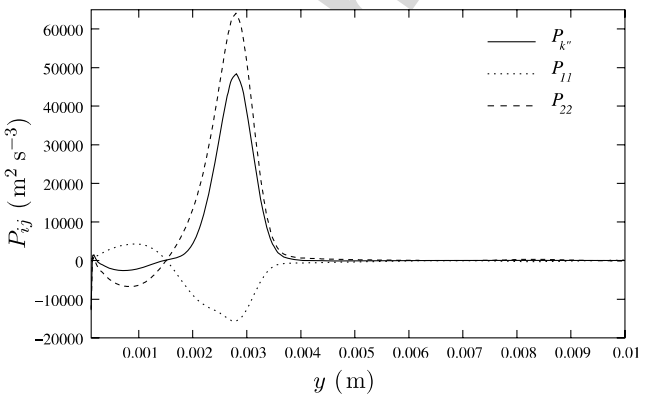

Fig. 10. Production tensor and $P_{k''}$ along the centreline ($x = 0$) at phase 60, Reynolds-stress model.

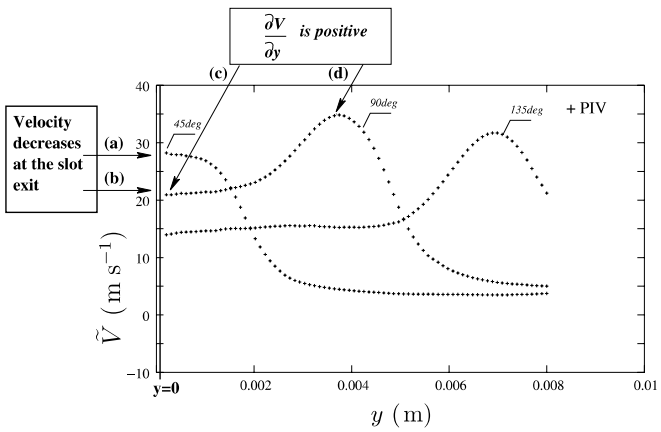

Fig. 11. PIV velocity profiles in the symmetry plane, at phase 45, 90, 135.

transient turbulent field shows a reduction of the Reynolds-stress tensor anisotropy. It is thus clear that in this two different flows, the combination of anisotropy in the jet and decrease of the velocity at the slot exit after the maximum necessarily implies negative production. Kinetic energy is thus transferred from turbulence to the oscillating motion through the component $\langle v''^2\rangle$. The other components $\langle u''^2\rangle$ and $\langle w''^2\rangle$ also lose their energy via redistribution to $\langle v''^2\rangle$.

The acceleration of the fluid particle observed in Fig. 6 is thus due to the fact that the third term in the RHS of Eq. (3), the shear stress, is not sufficient to balance the first two terms, in which the pressure gradient is dominant.

With the standard k''–ε'' model, which is unable to predict negative production, the picture is reversed: instead of providing energy to the oscillating motion, $\langle v''^2\rangle$ increases rapidly and this misprediction is sufficient to changes the sign of the momentum budget (Eq. (3)). The previously quoted increase of the peak velocity between phases 45 and 90 is then missed: the peak velocity is much too weak, as seen in Fig. 6, which leads to too short a penetration of the jet into the quiescent air.

Fig. 12 shows profiles of long-time averaged velocity V. Surprisingly, despite the strong overestimation of k'', shown in Fig. 15, the k''–ε'' model reproduces the spreading of the jet better than the RSM. This is a good example of the beneficial effect of the compensation of errors: basing the comparison of the relative performance of the models on long-time-averaged velocity profiles is clearly misleading.

The RSM also predicts regions of negative production at the periphery of the large eddies (Fig. 14a). A detailed analysis (not shown here) indicates that production in these regions are dominated by the first two terms in Eq. (4): $\langle u''^2\rangle - \langle v''^2\rangle$ is negative and $\partial V/\partial y$ is positive.

4.3. Misalignment of the strain and anisotropy tensors

It is well known that negative production results from a misalignment of the proper axes of the strain and anisotropy tensors: in particular, in flows subjected to periodic irrotational strains, a time lag is observed between these two tensors, which is at the origin of a turbulence decay

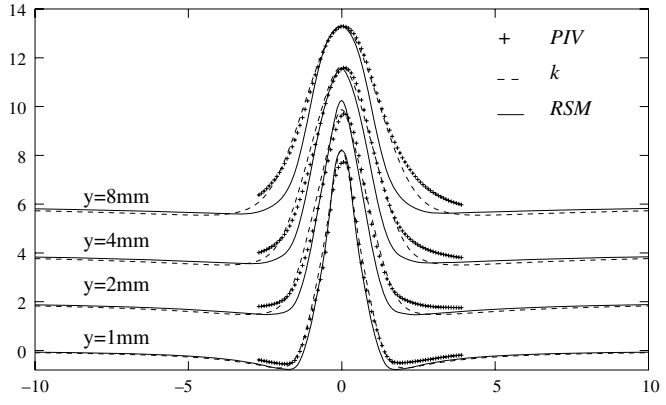

Fig. 12. Profiles of the long-time-averaged velocity V for different values of y.

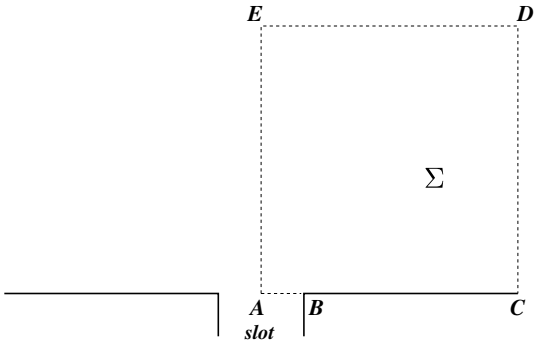

Fig. 13. Definition of the line used for the calculation of the circulation.

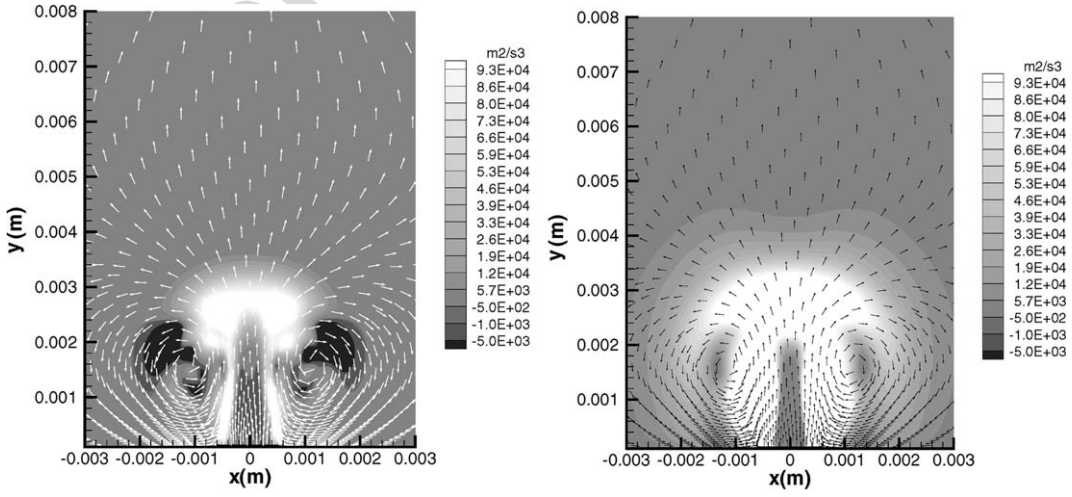

(a) RSM (b) k''–ε''

Fig. 14. Contours of $P_{k''}$ and velocity vectors at phase = 60.

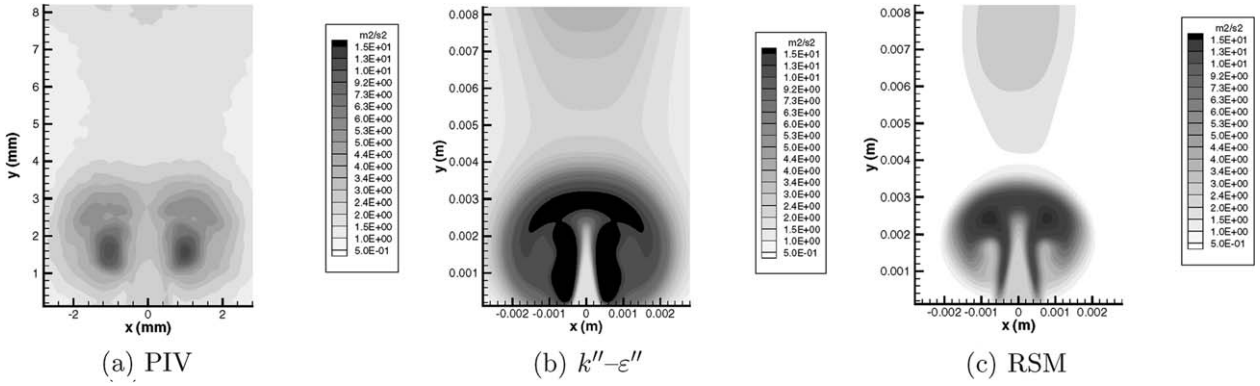

Fig. 15. Contours of k'' at phase = 60.

(see, e.g., Hadžić et al., 2001). The strain and anisotropy tensors are both 3×3 symmetrical tensors: the eigenvectors form orthogonal bases. Since the flow field is two dimensional, the third eigenvector is the same for both tensors and aligned with the z-axis. Let θ be the angle between the eigenvectors of the anisotropy tensor $\underline{\underline{a}}''$ and those of the strain tensor $\underline{\underline{\widetilde{S}}}$ in the x–y-plane, as shown in Fig. 16.

The anisotropy tensor $\underline{\underline{a}}''$, defined by $a''_{ij} = \langle u''_i u''_j \rangle / k'' - \frac{2}{3}\delta_{ij}$, can be written:

$$\underline{\underline{a}}'' = \begin{bmatrix} \lambda_1 & 0 & 0 \\ 0 & \lambda_2 & 0 \\ 0 & 0 & \lambda_3 \end{bmatrix} \tag{5}$$

in its own eigenaxes, where λ_i's are the three eigenvalues (with, arbitrarily, $\lambda_1 > \lambda_2 > \lambda_3$). In the same basis, the strain tensor reads:

$$\underline{\underline{\widetilde{S}}} = \begin{bmatrix} \widetilde{S}_{11} & \widetilde{S}_{12} & 0 \\ \widetilde{S}_{12} & \widetilde{S}_{22} & 0 \\ 0 & 0 & 0 \end{bmatrix} = \begin{bmatrix} -\beta\cos 2\theta & -2\beta\cos\theta\sin\theta & 0 \\ -2\beta\cos\theta\sin\theta & \beta\cos 2\theta & 0 \\ 0 & 0 & 0 \end{bmatrix} \tag{6}$$

where β is the positive eigenvalue of $\underline{\underline{\widetilde{S}}}$. Unlike eddy-viscosity models, the production term in RSM does not need modelling, and reads:

$$P_{k''} = -k\underline{\underline{a}}'' : \underline{\underline{\widetilde{S}}} = k\beta(\lambda_1 - \lambda_2)\cos 2\theta \tag{7}$$

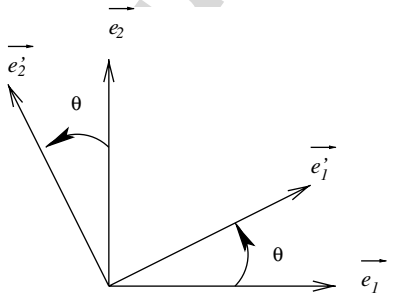

Fig. 16. Definition of the angle θ between the eigenvectors of $\underline{\underline{a}}''$ $(\vec{e_1}, \vec{e_2})$ and those of $\underline{\underline{\widetilde{S}}}$ $(\vec{e_1}', \vec{e_2}')$.

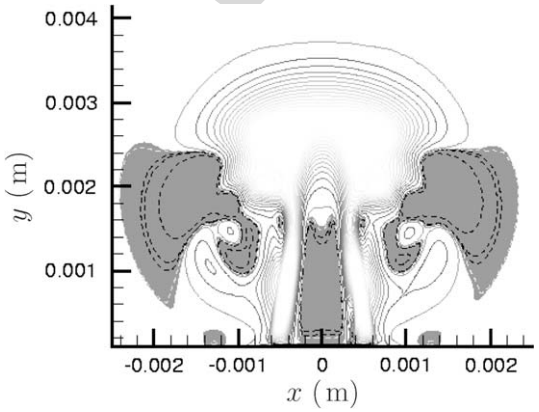

Fig. 17. Links between $P_{k''}$ (dashed lines = negative contours) and regions where $\theta > 45°$ (in grey).

For instance, in the symmetry plane, just above the slot exit, at phase 60 (Fig. 14), the eigenvalues of the anisotropy tensor are $\lambda_1 = a_{22}$ and $\lambda_2 = a_{11}$, and the eigenvectors are aligned with the y- and the x-axes, respectively. The positive eigenvalue of $\underline{\underline{\widetilde{S}}}$ is $\beta = \partial V/\partial y$, and its eigenvectors are aligned with x- and the y-axes, respectively, such that $\theta = 90°$, and the production is negative. Fig. 17 illustrates the correspondence between θ and the regions of negative production at phase 60.

The k''–ε'' model is of course unable to capture such a mechanism because the anisotropy and strain tensors are forced to be directly in phase, leading to an overestimation of turbulent kinetic energy, as shown in Fig. 15, which is in turn at the origin of the wrong prediction of the peak velocities, as shown in Section 4.2. Therefore, the stress-strain lag, whose role was emphasized by Hadžić et al. (2001) in the case of homogeneous turbulence subjected to periodic compression-dilatation strains, also plays a fundamental role in the present flow.

4.4. Vortex generation

Using standard vortex generation analysis, it can be shown that the vortex dipole created during a cycle is mainly driven by inviscid dynamics. Indeed, let Σ be the

part of the x–y-plane delimited by a the line $\partial\Sigma = ABCDE$, as shown in Fig. 13. The time-derivative of the circulation Γ along $\partial\Sigma$ is given by:

$$\frac{\partial\Gamma}{\partial t} = \oint_{\partial\Sigma} \frac{\partial\underline{\widetilde{U}}}{\partial t}\cdot \underline{\mathrm{d}\ell} = \int\int_{\Sigma} \frac{\partial\widetilde{\omega}}{\partial t}\,\mathrm{d}S \tag{8}$$

where the vorticity $\widetilde{\omega}$ is the component in the z-direction of the curl of the velocity vector $\nabla\times\underline{\widetilde{U}}$. In an inviscid 2D flow, the material derivative of vorticity is zero, such that:

$$\begin{aligned}\frac{\partial\Gamma}{\partial t} &= -\int\int_{\Sigma}\frac{\partial\widetilde{\omega}\widetilde{U}_k}{\partial x_k}\,\mathrm{d}S = -\oint_{\partial\Sigma}\widetilde{\omega}\widetilde{U}_k n_k\,\mathrm{d}\ell \\ &= -\int_0^{h/2}\widetilde{\omega}\widetilde{V}\,\mathrm{d}x\end{aligned} \tag{9}$$

where the third equation holds because BC is a wall, CD and DE are supposed sufficiently far from the blob of vorticity ($\widetilde{\omega}\simeq 0$), and $\widetilde{\omega}=0$ on the symmetry line EA. Just at the outlet of the slot, $\partial U/\partial y$ is small compared to $\partial V/\partial x$, such that Eq. (9) reduces to:

$$\frac{\partial\Gamma}{\partial t} = -\frac{\widetilde{V}_0^2}{2} \tag{10}$$

where $\widetilde{V}_0$ is the velocity at the centre of the slot ($x=0$).

The circulation along $\partial\Sigma$ predicted by a purely inviscid dynamics can thus be estimated at every time using Eq. (10), from the experimental value of $\widetilde{V}_0$. Now, using the Lamb–Oseen (Lamb, 1945) model for a vortex:

$$\widetilde{V}_\theta(r) = \frac{\Gamma}{2\pi r}\left(1-\mathrm{e}^{-r^2/R^2}\right) \tag{11}$$

an estimation of the velocity field is obtained (r and θ are the cylindrical coordinates with respect to the vortex centre). In Eq. (11), the only parameters that cannot be predicted by the inviscid theory are the location of the vortex centre and the radius of the vortex core R. In Fig. 18, the locations (x_0,y_0) and $(-x_0,y_0)$ of the centres of the vortices were determined from the PIV velocity field, and the velocity profiles were extracted at $y=y_0$. The radius of the vortex core R is then obtained from the velocity gradient $\partial V/\partial x$ at the centre of the vortices.

The velocity induced by the vortex dipole is the vectorial sum of the velocities induced by each vortex:

$$\widetilde{V}_\theta^{\mathrm{tot}} = \widetilde{V}_\theta(r) + \widetilde{V}_\theta(r^*) \tag{12}$$

where $r^{*2} = (x+x_0)^2 + (y-y_0)^2$. Taking the x-derivative of Eq. (12) at $(x=x_0, y=y_0)$, shows that R can be evaluated by:

$$\frac{1}{R^2} = \frac{2\pi}{\Gamma}\left(\left.\frac{\partial\widetilde{V}_\theta^{\mathrm{tot}}}{\partial x}\right|_{x_0,y_0} + \frac{\Gamma}{8\pi x_0^2}\right) \tag{13}$$

The excellent agreement in Fig. 18a of the Lamb–Oseen model with the experimental profile shows that, up to this phase, the vortices are mainly driven by an inviscid dynamics: despite a significant level of velocity fluctuations (above 5%), the flow is more transitional than fully turbulent when it issues from the slot. It is moreover difficult to estimate the relative contribution in the velocity fluctuations of the deviation from periodicity in the diaphragm motion. In Fig. 18b, it can be seen that the vorticity injected through the slot has partly been dissipated at phase 135. Since the radius of the vortex cores is not given by the inviscid theory but rather chosen to fit the profile, the Lamb–Oseen vortices still reproduce accurately the experiment in the region $-0.002\ \mathrm{m} < x < 0.002\ \mathrm{m}$. However, outside this region, it is observed that the inviscid theory predicts too strong a backflow, which shows that the circulation Γ is overestimated, since in this region, Eq. (11) goes asymptotically to $\widetilde{V}_\theta(r) = \Gamma/(2\pi r)$. This conclusion is completely independent of the particular choice of R.

In such a transitional region, what is expected from turbulence models is to influence the flow as little as possible. As shown in Section 4.2, the k''–ε'' model strongly overestimates the turbulent energy. Therefore, a strong viscous term is artificially added to the vorticity equation, and, in turn, introduced in Eq. (9). The circulation is then dissipated, which explains at the same time why the acceleration of the fluid particle on the centreline is missed and why the convection velocity is underestimated (Fig. 18 shows that

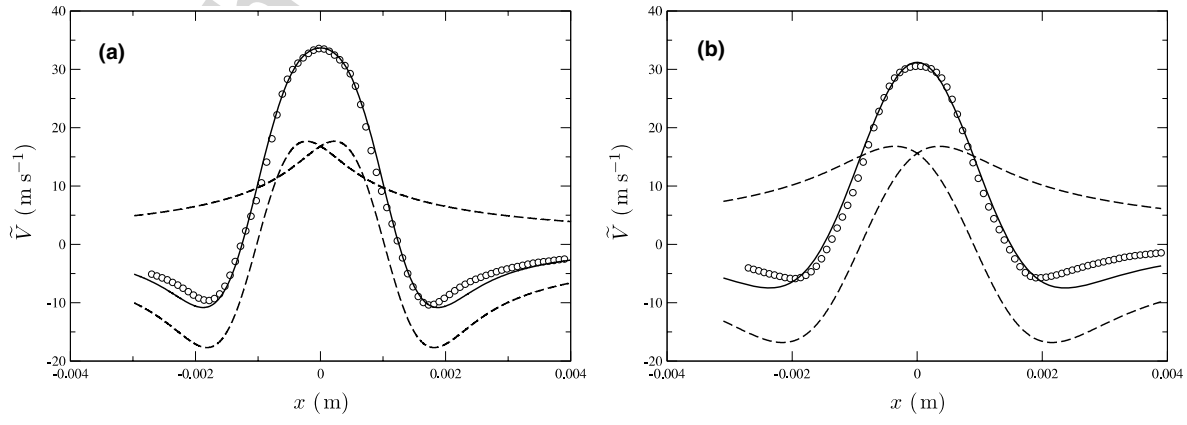

Fig. 18. Velocity profiles $\widetilde{V}(x)$ at (a): phase 90, $y_0 = 3.6$ mm; (b): phase 135, $y_0 = 6.6$ mm. (○) PIV data; (- - -) velocity induced by each vortex; (—) velocity induced by the vortex dipole.

the convection velocity is a consequence of mutual induction of the vortex dipole).

5. Conclusions

The turbulence rate of the synthetic jet studied in the present work is above 5% at the slot exit and can reach 20% around the vortex core, which could question the use of turbulence models. Indeed, despite this significant level of fluctuations, the analysis of the dynamics of the vortex dipole shows that the flow is more transitional than fully turbulent. Nevertheless, in industrial applications (Getin, 2000; Ben Chiekh et al., 2003; Amitay et al., 2001) synthetic jets interact with the developed turbulence of the flow to be controlled: therefore, a turbulence model must be able to reproduce the dynamics of the synthetic jet region as well as the fully turbulent region. This is very challenging for statistical modelling.

The present work was dedicated to the investigation of the relative performance of two closure levels: eddy-viscosity and Reynolds-stress models. The solutions are free from turbulent eddies (i.e., represent only the oscillating motion), which shows that the standard models derived for statistically steady flows can also be suitable for flows treated in phase averaging.

However, the results clearly demonstrate the superiority of the Reynolds-stress model. Indeed, the k''–ε'' model severely alters the evolution of the vortex dipole: the generation of the large-scale periodic contra-rotating vortices are directly inherited from the inviscid dynamics, but their dissipation and their convection velocity are driven by the level of viscosity (molecular and turbulent). The k''–ε'' model predicts a much too high turbulence energy, a rapid decrease of the peak velocity, and, consequently, too short a penetration of the jet into quiescent air. The Reynolds-stress model gives a much more realistic solution, but slightly underestimates the peak velocities, the convection velocity and the spreading rate of the jet.

The analysis of the turbulence production mechanisms shows that the discrepancies between the two models can be traced to the presence, during the deceleration phase, of a region of negative production that plays a crucial role in the global dynamics of the flow. Such a negative-production region is due to the combination of the anisotropy of turbulence in the jet and the positive gradient of velocity in the streamwise direction, which are both present in every pulsed jet. Since the k''–ε'' model is not able to account for the stress-strain lag at the origin of the negative production, it predicts an erroneous, intense increase of turbulent energy, which is sufficient to change the sign of the momentum budget.

The present study clearly pleads against the use of linear eddy-viscosity models for this type of flows. Rumsey et al. (2004) arrived at the opposite conclusion by synthesizing the results of the *2004 CFD validation workshop on synthetic jets and turbulent separation control*: they concluded that linear eddy-viscosity models produce the best results among URANS models, whatever the formulation used (SA, standard k–ε, SST).

Indeed comparisons of long-time-averaged quantities are misleading, because of compensation of errors. When phase-averaged quantities are compared in details, the deficiencies of linear eddy-viscosity models clearly appear. In order to evaluate the ability of the models to reproduce the unsteady dynamics of the flow, it is much more relevant to focus on the behaviour of the vortex dipole, in terms of location, intensity, convection velocity and penetration into the ambient fluid: the Reynolds-stress model is able to reproduce the correct dynamics, contrary to the k''–ε'' model.

However, since the turbulence is far from equilibrium in the region close to the slot exit, it is also difficult for a Reynolds-stress model to reproduce accurately the interaction between the turbulence and the vortex dipole. Bremhorst et al. (2003) showed the beneficial effect of multiscale k''–ε'' modelling in an axisymmetric pulsed jet. Their study, together with the present study, suggests to investigate the performance of multiscale Reynolds-stress models (e.g.,Schiestel, 1987; Cadiou et al., 2004).

Acknowledgements

The authors gratefully acknowledge Jacques Borée for many useful discussions during the course of the present research project.

References

Amitay, M., Smith, D.R., Kibens, V., Parekh, D.E., Glezer, A., 2001. Modification of the aerodynamics characteristics of an unconventional airfoil using synthetic jet actuators. AIAA J. 39 (3), 361–370.

Archambeau, F., Mehitoua, N., Sakiz, M., 2004. Code Saturne: A finite volume code for the computation of turbulent incompressible flows – industrial applications. Int. J. Finite Volume, Electronical edition: <http://averoes.math.univ-paris13.fr/html>, ISSN 1634 (0655).

Aubrun, S., Kao, P.L., Ha Minh, H., Boisson, H., 1999. The semi-deterministic approach as way to study coherent structures. Case of a turbulent flow behind a backward-facing step. In: Proc. fourth Int. Symp. Engng. Turb. Modelling and Measurements, Ajaccio, Corsica, France, pp. 491–499.

Bastin, F., Lafon, P., Candel, S., 1997. Computation of jet mixing noise due to coherent structures: the plane jet case. J. Fluid Mech. 335, 261–304.

Batten, P., Goldberg, U., Chakravarthy, S., 2002. LNS – an approach towards embedded LES. AIAA Paper 2002-0427, AIAA 40th Aerospace Sciences Meeting and Exhibit, Reno, Nevada.

Ben Chiekh, M., Béra, J.-C., Sunyach, M., 2003. Synthetic jet control for flows in a diffuser: vectoring, spreading and mixing enhancement. J. Turbulence 4.

Benhamadouche, S., Laurence, D., 2003. LES, coarse LES, and transient RANS. Comparisons on the flow across a tube bundle. Int. J. Heat Fluid Flow 24, 470–479.

Borée, J., Atassi, N., Charnay, G., Tauber, L., 1997. Measurements and image analysis of the turbulent field in an axisymmetric jet subject to a sudden velocity decrease. Exp. Thermal Fluid Sci. 14 (1), 45–51.

Bosch, G., Rodi, W., 1996. Simulation of vortex shedding past a square cylinder near a wall. Int. J. Heat Fluid Flow 17, 267–275.

Bremhorst, K., Craft, T. J., Launder, B. E., 2003. Two-time-scale turbulence modelling of a fully-pulsed axisymmetric air jet. In: Proc.

3rd Int. Symp. Turb. Shear Flows and Phenomena, Sendai, Japan, pp. 711–716.

Cadiou, A., Hanjalic, K., Stawiarski, K., 2004. A two-scale second-moment turbulence closure based on weighted spectrum integration. Theor. Comput. Fluid Dyn. 18 (1), 1–26.

Carpy, S., Manceau, R., 2006. Movies associated to the paper: Turbulence modelling of statistically periodic flows: synthetic jet into quiescent air. Available from: <http://labo.univ-poitiers.fr/informations-lea/CarpyManceauIJHFF2006/Index.html>.

Chaouat, B., Schiestel, R., 2005. A new partially integrated transport model for subgrid-scale stresses and dissipation rate for turbulent developing flows. Phys. Fluids 17 (065106), 1–19.

Durbin, P.A., 1995. Separated flow computations with the k–ε–$\overline{v^2}$ model. AIAA J 33, 659–664.

Gatski, T.B., 2001. DNS/LES for NASA aerodynamic needs and engineering applications. In: Liu, C., Sakell, L., Beutner, T. (Eds.), DNS/LES – Progress and Challenges. Greyden Press, Columbus, OH, pp. 25–34.

Getin, N., 2000. Simulation numérique du contro(le actif par jet pulsés de l'écoulement turbulent autour d'un cylindre circulaire. Ph.D. thesis, Ecole Centrale de Lyon.

Girimaji, S.S., Srinivasan, R., Jeong, E., 2003. PANS turbulence model for seamless transition between RANS and LES: fixed-point analysis and preliminary results. In: Proc. 4th ASME_JSME Joint Fluids Engineering Conference, Honolulu, Hawaii, USA.

Greenblatt, D., Wygnanski, I., 2000. Control of flow separation by periodic excitation. Progress Aerospace Sci. 36 (7), 487–545.

Ha Minh, H., Kourta, A., 1993. Semi-deterministic modelling for flows dominated by strong organized structures. In: Proc. 9th Int. Symp. Turbulent Shear Flows, Kyoto, Japan.

Hadžić, I., Hanjalić, K., Laurence, D., 2001. Modeling the response of turbulence subjected to cyclic irrotational strain. Phys. Fluids 13 (6), 1739–1747.

Hassan, A.A., Janakiram, R.D., 1997. Effects of zero-mass synthetic jets on the aerodynamics of the NACA-0012 airfoil. AIAA Paper 97-2326.

Iaccarino, G., Durbin, P., 2000. Unsteady 3D RANS simulations using the v^2–f model. In: Ann. Res. Briefs. Center for Turbulence Research, Stanford University, pp. 263–269.

Jin, G., Braza, M., 1994. Two-equation turbulence model for unsteady separated flows around airfoils. AIAA J. 32 (11), 2316–2322.

Johansson, S., Davidson, L., Olsson, E., 1993. Numerical simulation of vortex shedding past triangular cylinders at high Reynolds number using a k–ε turbulence model. Int. J. Numer. Meth. Fluids 16 (10), 859–878.

Kenjereš, S., Gunarjo, S., Hanjalić, K., 2005. Contribution to elliptic relaxation modelling of turbulent natural and mixed convection. Int. J. Heat Fluid Flow 26 (4), 569–586.

Kenjereš, S., Hanjalić, K., Krstović, G., 2001. Combined effects of terrain orography and thermal stratification on pollutant distribution in a town valley: a T-RANS simulation. In: Proc. 2nd Int. Symp. Turb. Shear Flow Phenomena, vol. 1, Stockholm, Sweden, pp. 103–108.

Lamb, H., 1945. Hydrodynamics. Dover, New-York.

Lardeau, S., Leschziner, M.A., 2005. Unsteady RANS modelling of wake-blade interaction: computational requirements and limitations. Comput. Fluids 34, 3–21.

Lasher, W.C., Taulbee, D.B., 1992. On the computation of turbulent backstep flow. Int. J. Heat Fluid Flow 13, 30–40.

Launder, B.E., Reece, G.J., Rodi, W., 1975. Progress in the development of a Reynolds-stress turbulence closure. J. Fluid Mech. 68 (3), 537–566.

Launder, B.E., Spalding, D.B., 1974. The numerical computation of turbulent flows. Comput. Meth. Appl. Mech Engng. 3 (2), 269–289.

Menter, F.R., Egorov, Y., 2005. SAS turbulence modelling of technical flows. In: Proc. 6th ERCOFTAC Workshop on Direct and Large-Eddy Simulation, Poitiers–Futuroscope, France.

Rumsey, C.L., Gatski, T.B., Sellers, W.L., Vatsa, V.N., Viken, S.A., 2004. Summary of 2004 CFD validation workshop on synthetic jets and turbulent separation control. In: Second AIAA Flow Control Conference, Portland, OR, USA (AIAA–2004–2217). Available from: <http://cfdval2004.larc.nasa.gov>.

Schiestel, R., 1987. Multiple-time-scale modeling of turbulent flows in one-point closures. Phys. Fluids 30 (3), 722–731.

Schiestel, R., Dejoan, A., 2005. Towards a new partially integrated transport model for coarse grid and unsteady turbulent flow simulations. Theor. Comput. Fluid Dyn. 18 (6), 443–468.

Seifert, A., Bachar, T., Koss, D., Shepshelovich, M., Wygnanski, I., 1993. Oscillatory blowing. a tool to delay boundary-layer separation. AIAA Paper 31-2052.

Sellers, W.L., Rumsey, C.L., 2004. Langley Research Center workshop on CFD validation of synthetic jets and turbulent separation control. Available from: <http://cfdval2004.larc.nasa.gov>.

Spalart, P., Jou, W.-H., Strelets, M., Allmaras, S., 1997. Comments on the feasibility of LES for wings, and on a hybrid RANS/LES approach. In: Liu, C., Liu, Z. (Eds.), First AFOSR International Conference on DNS/LES, 4–8 August, Ruston, LA, Advances in DNS/LES. Greyden Press, Columbus, OH, USA.

Speziale, C.G., 1998. Turbulence modeling for time-dependent RANS and VLES: a review. AIAA J. 36 (2), 173.

Stawiarski, K., Hanjalić, K., 2002. A two-scale second-moment one-point turbulence closure. In: Proc. 5th Int. Symp. Engng Turb. Modelling and Measurements, Mallorca, Spain.

Tardu, S., Da Costa, P., 2005. Experiments and modeling of an unsteady turbulent channel flow. AIAA J. 43 (1), 140–148.

Yao, C., Chen, F.J., Neuhart, D., Harris, J., 2004. Synthetic jet flow field database for CFD validation. AIAA Paper 2004-2218.